Monthly Notices of the ROYAL ASTRONOMICAL SOCIETY

MNRAS **466,** 892–905 (2017) doi:10.1093/mnras/stw3120
Advance Access publication 2016 December 1

SINFONI-HiZELS: the dynamics, merger rates and metallicity gradients of 'typical' star-forming galaxies at $z = 0.8$–2.2

J. Molina,[1]★ Edo Ibar,[2] A. M. Swinbank,[3,4] D. Sobral,[5,6] P. N. Best,[7] I. Smail,[3,4] A. Escala[1] and M. Cirasuolo[7,8]

[1]*Departamento de Astronomía, Universidad de Chile, Casilla 36-D, Santiago, Chile*
[2]*Instituto de Física y Astronomía, Universidad de Valparaíso, Avda. Gran Bretaña 1111, Valparaíso, Chile*
[3]*Centre for Extragalactic Astronomy, Department of Physics, Durham University, South Road, Durham DH1 3LE, UK*
[4]*Institute for Computational Cosmology, Durham University, South Road, Durham DH1 3LE, UK*
[5]*Department of Physics, Lancaster University, Lancaster LA1 4YB, UK*
[6]*Leiden Observatory, Leiden University, P.O. Box 9513, NL-2300 RA Leiden, the Netherlands*
[7]*SUPA, Institute for Astronomy, Royal Observatory, Blackford Hill, Edinburgh EH9 3HJ, UK*
[8]*European Southern Observatory, Karl-Schwarzschild-Strasse 2, D-85748 Garching bei Muenchen, Germany*

Accepted 2016 November 29. Received 2016 November 28; in original form 2016 September 20

ABSTRACT

We present adaptive optics (AO) assisted SINFONI integral field unit (IFU) spectroscopy of 11 Hα emitting galaxies selected from the High-Z Emission Line Survey (HiZELS). We obtain spatially resolved dynamics on ∼kpc-scales of star-forming galaxies [stellar mass $M_\star = 10^{9.5-10.5}$ M$_\odot$ and star formation rate (SFR) = 2–30 M$_\odot$ yr^{-1}] near the peak of the cosmic star formation rate history. Combining these observations with our previous SINFONI-HiZELS campaign, we construct a sample of 20 homogeneously selected galaxies with IFU AO-aided observations – the 'SHiZELS' survey, with roughly equal number of galaxies per redshift slice, at $z = 0.8$, 1.47 and 2.23. We measure the dynamics and identify the major kinematic axis by modelling their velocity fields to extract rotational curves and infer their inclination-corrected rotational velocities. We explore the stellar mass Tully–Fisher relationship, finding that galaxies with higher velocity dispersions tend to deviate from this relation. Using kinemetry analyses, we find that galaxy interactions might be the dominant mechanism controlling the star formation activity at $z = 2.23$ but they become gradually less important down to $z = 0.8$. Metallicity gradients derived from the [N II]/Hα emission line ratio show a median negative gradient for the SHiZELS survey of $\Delta\log(\mathrm{O/H})/\Delta R = -0.026 \pm 0.008$ dex kpc^{-1}. We find that metal-rich galaxies tend to show negative gradients, whereas metal-poor galaxies tend to exhibit positive metallicity gradients. This result suggests that the accretion of pristine gas in the periphery of galaxies plays an important role in replenishing the gas in 'typical' star-forming galaxies.

Key words: galaxies: abundances – galaxies: evolution – galaxies: high-redshift – galaxies: interactions – galaxies: ISM – galaxies: star formation.

1 INTRODUCTION

Determining the physical processes that control star formation and mass assembly at high redshift is an area of intense debate. At $z = 1$–2, galaxies were actively forming stars and rapidly growing their stellar mass content (e.g. Madau et al. 1996; Sobral et al. 2009a). However, studies also found a strong decline in star formation rate (SFR) from that epoch to the present day: the cosmic SFR density of the Universe has dropped by more than an order of magnitude (e.g. Gilbank et al. 2011; Karim et al. 2011; Rodighiero et al. 2011; Sobral et al. 2013b). The primary causes of the subsequent decline of the star formation rate activity since $z = 1$–2 is still under debate.

Two main explanations have emerged to explain how galaxies maintained such high levels of star formation at those redshifts: (1) the rate of mergers and tidal interactions may have been higher at that epoch, driving quiescent discs into bursts of star formation (e.g. Bridge et al. 2007; Conselice, Yang & Bluck 2009); and (2) galaxies were continuously fed gas from the intergalactic medium (IGM), promoting and maintaining star formation activity driven by internal

★ E-mail: jumolina@das.uchile.cl

dynamical processes within the interstellar medium (ISM; e.g. Keres et al. 2005; Bournaud & Elmegreen 2009; Dekel et al. 2009a).

To test the predictions from these galaxy evolution models, a method for distinguishing between mergers and galaxy discs needs to be implemented. Three main methods of estimating the merger fraction are: counting close pairs of galaxies, assuming that they will subsequently merge (e.g. Lin et al. 2008; Bluck et al. 2009); using a method of identifying galaxies with merging morphology (e.g. Conselice et al. 2003; Conselice, Rajgor. & Mywers 2008; Conselice 2009; Lotz et al. 2008; Stott et al. 2013a); and employing detailed integral field unit (IFU) spectroscopy to look for dynamical merger signatures (e.g. Shapiro et al. 2008; Förster Schreiber et al. 2009; Bellocchi, Arribas & Colina 2012; Contini et al. 2012; Swinbank et al. 2012a).

If secular processes drive the galaxy discs evolution, we need to measure the internal dynamical properties of galaxies at the peak epoch of the volume-averaged SFR, constrain how the structural properties of galaxy discs have varied over cosmic time and test if the prescriptions developed to understand the star formation processes at $z = 0$ are still valid in the ISM of galaxies at high-z.

Taking advantage of IFU adaptive optics (AO) assisted observations, significant effort has been invested to measure the kinematics of the gas within star-forming galaxies at $z \sim 1$–2 in order to test competing models for galaxy growth (see review by Glazebrook 2013). Previous observations have shown highly turbulent, rotationally supported discs with clumpy star formation and large gas fractions ($f_{\rm gas}$ = 20–80 per cent; Elmegreen et al. 2009; Förster Schreiber et al. 2009; Genzel et al. 2010; Geach et al. 2011; Wisnioski et al. 2011; Swinbank et al. 2012b; Stott et al. 2016). Higher gas fractions might lead the formation of massive ($\sim 10^9$ M$_\odot$) clumps by gravitational fragmentation of dynamically unstable gas (Escala & Larson 2008). The typical rotation velocities of these systems are 100–300 km s^{-1}, so very similar to local galaxies (Cresci et al. 2009; Gnerucci et al. 2011b; Vergani et al. 2012; Swinbank et al. 2012a), but the typical velocity dispersion values range from 50 to 100 km s^{-1} (Förster Schreiber et al. 2006; Genzel et al. 2006). This means a circular velocity to velocity dispersion ratio (V/σ) range from 1 to 10 at $z \sim 2$ (van Starkenburg et al. 2008; Förster Schreiber et al. 2009; Law et al. 2009; Genzel et al. 2011; Gnerucci et al. 2011b; Stott et al. 2016). By comparison, the Milky Way and other similar thin discs galaxies at low-z have $V/\sigma \sim$ 10–20 (Bershady et al. 2010; Epinat et al. 2010). This suggests that the gas dynamics of high-z galaxies are not just dominated by ordered rotation or random motions, but by a contribution from both.

If the structural properties of galaxy discs have varied over cosmic time, we would expect to see evidence in kinematic scaling relations. For example, one potential evidence would be an evolution of the Tully–Fisher relationship (Tully & Fisher 1977), which describes the interdependence of baryonic and dark matter in galaxies by studying the evolution of the stellar luminosity ($M_{\rm B}$) versus circular velocity. It traces a simple means of the build-up of galaxy discs at different epochs. Since the B-band luminosity is sensitive to recent star formation, attempts have also been made to measure the evolution of the stellar mass ($M_\star$) Tully–Fisher relation (TFR) that reflects the relation between the past-average star formation history and halo mass. In particular, hydrodynamic models suggest that the zero-point of the stellar mass Tully–Fisher relationship should evolve by ~ -1.1 dex at fixed circular velocity between $z = 0$ and 2 (McCarthy et al. 2012). At a given rotational velocity, the stellar mass in a high-z disc galaxy should be smaller than a low-z disc galaxy as star formation builds it up. Substantial efforts have been made in order to measure the Tully–Fisher relationship at redshift $z = 1$–2 (Cresci et al. 2009; Förster Schreiber et al. 2009; Gnerucci et al. 2011b; Miller et al. 2011, 2012; Swinbank et al. 2012a; Sobral et al. 2013b; Di Teodoro, Fraternali & Miller 2016; Tiley et al. 2016). Recently, Tiley et al. (2016) have measured a stellar-mass TFR zero-point evolution of -0.41 ± 0.08 dex for rotationally supported galaxies defined with $V/\sigma > 3$ from the 'KMOS Redshift One Spectroscopic Survey' (KROSS; Stott et al. 2016). However, they measure no significant offset in the absolute rest-frame K-band TFR (M_K–TFR) over the same period. This excess of K-band luminosity at fixed stellar mass measured from the high-z galaxies could be explained by considering their higher SFRs in comparison with their local Universe counterparts at same stellar mass. The excess of light that comes from young stars decreases the mass-to-light ratio in high-z galaxies decoupling the evolution of both, the M_K–TFR and the $M_\star$–TFR.

If the Tully–Fisher relationship evolves with redshift, then it would be expected that the galaxy size–velocity relation also evolves (Dutton et al. 2011b). In a Λ cold dark matter (ΛCDM) cosmology, the sizes of galaxy discs and their rotational velocities should be proportional to their parent dark matter haloes, and since the haloes are denser at high-z for a fixed circular velocity, then disc sizes should scale inversely with Hubble time (Mo, Mao & White 1998). The evolution of the size–velocity relation has been observed (Swinbank et al. 2012a), but increasing the number statistics should be helpful in order to overcome random errors due to different methods and conversions of size measurements.

A third potential observational tool to constrain galaxy evolution models is the measure of the chemical abundance within galaxies using a simple disc model. If the gas accretion in high-redshift galaxies is via accretion of pristine gas from the IGM along filaments on to the galaxy disc at 10–20 kpc from the galaxy centre, then the inner discs of galaxies should be enriched by star formation and supernovae whilst the outer disc is continually diluted by pristine material, leaving strong negative abundance gradients (Dekel et al. 2009a; Dekel, Sari & Ceverino 2009b). This gradient would flatten if the IGM gas is redistributed, e.g. via merger interactions.

To chart the evolution of star-forming galaxies with cosmic time, we exploit the panoramic (degree-scale) High-Z Emission Line Survey (HiZELS). This survey targets Hα emitting galaxies in four precise ($\delta z = 0.03$) redshift slices: $z = 0.4$, 0.8, 1.47 and 2.23 (Geach et al. 2008; Sobral et al. 2009a, 2010, 2011, 2012, 2013b). This survey provides a large luminosity-limited sample of homogeneously selected Hα emitters at the cosmic star formation density peak epoch, and provides a powerful resource for studying the properties of starburst galaxies and the star-forming galaxies that shows a tight dependence of SFR on stellar mass, the so-called 'main-sequence' of star-forming galaxies (Noeske et al. 2007; Pannella et al. 2009; Elbaz et al. 2011). Most of the HiZELS galaxies will likely evolve into $\sim L^*$ galaxies by $z = 0$ (Sobral et al. 2011), but are seen at a time when they are assembling most of their stellar mass, and thus are seen at a critical stage in their evolutionary history.

In this paper, we present AO-assisted integral field spectroscopy with SINFONI, yielding $\sim$0.15 arcsec resolution ($\sim$kpc scale), of 11 star-forming galaxies selected from the HiZELS survey in three redshift slices, $z = 0.8$, 1.47 and 2.23 (Sobral et al. 2013a). The HiZELS survey is based on observations obtained using the Wide Field Camera on the 3.8-m United Kingdom Infrared Telescope (Geach et al. 2008; Sobral et al. 2009a). Combined with nine targets from a previous similar SINFONI campaign (Swinbank et al. 2012a,b), our study present one of the largest samples of homogeneously selected high-redshift star-forming galaxies with AO-aided resolved

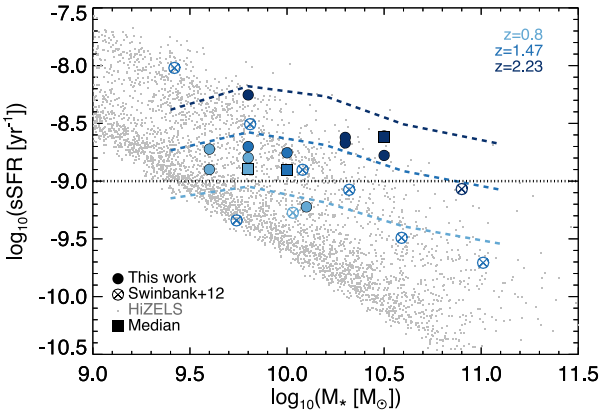

Figure 1. The relation between specific star formation rate (sSFR) and stellar mass for the HiZELS survey (grey dots; Sobral et al. 2013a, 2014), Swinbank et al. (2012a)'s sample (circles with X) and our sample (filled circles). We colour-coded our sample and the Swinbank et al. (2012a) sample by redshift. The sky blue, blue and dark blue colours represent the sources at $z = 0.8$, 1.47, 2.23, respectively. The filled squares represent the median values per redshift. The black dotted line shows the sSFR $=10^{-9}$ yr^{-1} value. The colour-coded dashed lines represent the location of the 'main sequence' of star-forming galaxies at each redshift slice from Karim et al. (2011) demonstrating that our sample and Swinbank et al. (2012a)'s sample are 'typical' for each epoch.

dynamics, star formation and chemical properties. Throughout the paper, we assume a ΛCDM cosmology with $\Omega_\Lambda = 0.73$, $\Omega_m = 0.27$, and $H_0 = 72$ km s^{-1} Mpc^{-1}, so at redshift $z = 0.8$, 1.47 and 2.23, a spatial resolution of 0.1 arcsec corresponds to a physical scale of 0.74, 0.84 and 0.82 kpc, respectively.

2 SAMPLE SELECTION, OBSERVATIONS AND DATA REDUCTION

2.1 HiZELS

To select the targets for IFU observations, we exploited the large sample of sources from the HiZELS imaging of the COSMOS, SA22 and UDS fields (Best et al. 2013; Sobral et al. 2013b, 2015, 2016a) to select Hα emitters sampling the so called 'main-sequence' at $z = 0.8$–2.23 (Fig. 1). Taking the advantage of the large sample, we could select galaxies that lie close (<30 arcsec) to bright ($R < 15.0$) stars, such that natural guide star AO correction (NGS correction) could be applied to achieve high spatial resolution. For this programme, we selected 18 galaxies with stellar mass between $M_\star = 10^{9.5-10.5}$ M$_\odot$ and Hα fluxes greater than $f_{H\alpha} \geq 0.7 \times 10^{-16}$ erg s^{-1} cm^{-2} to ensure that their star formation properties and dynamics could be mapped in a few hours. Out of the 18 galaxies observed with SINFONI, we detect 11 of them with high enough signal-to-noise (S/N) ratio. Given the significant sky-noise in near-IR spectra, source detection was optimally performed by detailed visual inspection of dynamical and line width features within the data cubes (using Interactive Data Language and QFitsView). Although the rate of detection of bright Hα emitters derived from our sample may seem modest (∼60 per cent), it is comparable with the detection rate derived from the previous SINFONI campaign (∼65 per cent; Swinbank et al. 2012a). We note that both samples were drawn from the same HiZELS survey. We note, however, that the detection rate derived from the non-AO KROSS survey (using KMOS; Stott et al. 2016) – which was also drawn from the HiZELS survey at $z \sim 0.8$ – is nearly ∼92 per cent. This suggests that the modest rate of detection derived from our sample and the previous SINFONI campaign might be inherent to the AO observations.

2.2 SINFONI observations

To measure the dynamics of our sample from the nebular Hα emission line, we used the SINFONI IFU (Eisenhauer et al. 2003) on the European Southern Observatory Very Large Telescope [Project 092.A-0090(A); P.I. E.Ibar]. We use the 3 arcsec × 3 arcsec field of view at spatial resolution of 0.1 arcsec pixel^{-1}. At $z = 0.8$, 1.47 and 2.23, the Hα emission line is redshifted to ∼1.18, 1.61 and 2.12 μm and into the *J*, *H* and *K* bands, respectively. The spectral resolution in each band is $\lambda/\Delta\lambda \sim 3700$, and sky OH lines are considerably narrower (∼4 Å full width half-maximum – FWHM) compared to the galaxy line widths. We use an NGS correction since each target is close to a bright guide star.

The observational setup for these targets was done in the same manner as in Swinbank et al. (2012a). To observe the targets, we used ABBA chop sequences (observational blocks with individual exposures of 600 s), nodding 1.6 arcsec across the IFU. In order to achieve higher S/N ratios on sources at higher redshifts, we used 2, 3, 4 OB's for the $z = 0.8$, 1.47, 2.23 samples implying a total observing time of 4.8, 7.2, 9.6 ks, respectively. The observations were carried between 2013 October 27 and 2014 September 3 in ∼0.8 arcsec seeing and photometric conditions. The median Strehl achieved for our observations is 33 per cent (Table 1).

Individual exposures were reduced using the SINFONI ESOREX data reduction pipeline that extracts flat-fields, wavelength calibrates and forms the data cubes for each exposure. The final data cube was generated by aligning manually the individual OBs on average (shifting them by $\lesssim$0.2 arcsec ∼ 2 pixels) and then combining these using a sigma-clipping average at each pixel and wavelength. This minimized the effect of the OH emission/absorption features seen in the final data cube.

2.3 Stellar masses

Stellar masses are computed by fitting spectral energy distributions (SEDs) to the rest-frame UV, optical and near-infrared data available (FUV, NUV, *U*, *B*, *g*, *V*, *R*, *i*, *I*, *z*, *Y*, *J*, *H*, *K*, 3.6, 4.5, 5.8 and 8.0 μm collated in Sobral et al. 2014, and references therein), following Sobral et al. (2011). The SED templates were generated with the Bruzual & Charlot (2003) package using Bruzual (2007) models, a Chabrier (2003) IMF and an exponentially declining star formation history with the form $e^{-t/\tau}$, with τ in the range 0.1–10 Gyr. The SEDs were generated for a logarithmic grid of 200 ages (from 0.1 Myr to the maximum age at each redshift being studied). Dust extinction was applied to the templates using Calzetti, Armus & Bohlin (2000) extinction law with $E(B-V)$ in the range 0–0.5 (in steps of 0.05) roughly corresponding to a Hα extinction $A_{H\alpha}$ ∼ 0–2 mag. The models are generated with different metallicities, including solar (Sobral et al. 2011). For each source, the stellar mass and the dust extinction are computed as the median values of the 1σ best fits over the range of parameters (see Table 1).

2.4 Star formation rates

The star formation rates of the sample are measured from the Hα emission line flux calculated from the HiZELS survey. Adopting the Kennicutt (1998) calibration and assuming a Chabrier IMF, the SFRs are given by $SFR^{obs}_{H\alpha}(M_\odot\ yr^{-1}) = 4.6 \times 10^{-42}\ L^{obs}_{H\alpha}(erg\ s^{-1})$. At the three redshift ranges of our sample, the average Hα fluxes

Table 1. Integrated galaxy properties. Flux densities ($f_{H\alpha}$) are taken from narrow-band photometry and include contamination by [N II]. $SFR^{obs}_{H\alpha}$ are not corrected for extinction. $r_{1/2}$ is the Hα half-light radius and has been deconvolved by the point spread function (PSF).

ID	RA (J2000)	Dec. (J2000)	Strehl	$z_{H\alpha}$	$f_{H\alpha}$ ($\times 10^{-16}$ erg s^{-1}cm^{-2})	[N II]/Hα	$SFR^{obs}_{H\alpha}$ ($M_\odot$ yr^{-1})	$\log_{10}(M_*)$ ($M_\odot$)	$r_{1/2}$ (kpc)	$E(B-V)$	$\Delta\log(O/H)/\Delta R$ (dex kpc^{-1})
SA22-17	22 19 36.1	+00 34 07.8	34 per cent	0.8114	1.7 ± 0.1	<0.1	2	9.6 ± 0.1	4.2 ± 0.3	0.5 ± 0.2	...
SA22-26	22 18 22.9	+01 00 22.1	34 per cent	0.8150	2.3 ± 0.2	0.26 ± 0.05	3	9.6 ± 0.2	3.1 ± 0.4	0.2 ± 0.2	−0.05 ± 0.02
SA22-28	22 15 36.3	+00 41 08.8	37 per cent	0.8130	2.6 ± 0.2	0.30 ± 0.06	4	9.8 ± 0.3	3.1 ± 0.3	0.5 ± 0.1	−0.03 ± 0.02
SA22-54	22 22 23.0	+00 47 33.0	21 per cent	0.8093	2.3 ± 0.1	0.12 ± 0.07	3	10.1 ± 0.2	2.4 ± 0.3	0.2 ± 0.1	...
COS-16	10 00 49.0	+02 44 41.1	32 per cent	1.3598	1.0 ± 0.1	0.10 ± 0.04	5	9.8 ± 0.3	1.5 ± 0.4	0.0 ± 0.1	+0.08 ± 0.02
COS-30	09 59 11.5	+02 23 24.3	21 per cent	1.4861	1.1 ± 0.1	0.43 ± 0.03	7	10.0 ± 0.1	3.5 ± 0.3	0.5 ± 0.1	−0.014 ±0.005
SA22-01	22 19 16.0	+00 40 36.1	25 per cent	2.2390	1.0 ± 0.1	0.42 ± 0.13	17	10.3 ± 0.4	2.0 ± 0.2	0.1 ± 0.1	...
SA22-02	22 18 58.9	+00 05 58.3	35 per cent	2.2526	1.2 ± 0.1	0.27 ± 0.07	21	10.5 ± 0.4	3.8 ± 0.3	0.0 ± 0.1	−0.005 ± 0.009
UDS-10	02 16 45.8	−05 02 44.7	33 per cent	2.2382	1.1 ± 0.1	0.23 ± 0.04	19	10.3 ± 0.1	1.6 ± 0.1	0.2 ± 0.1	...
UDS-17	02 16 55.3	−05 23 35.5	12 per cent	2.2395	1.8 ± 0.2	<0.1	31	10.5 ± 0.1	1.5 ± 0.3	0.3 ± 0.1	...
UDS-21	02 16 49.0	−05 03 20.6	33 per cent	2.2391	0.8 ± 0.1	<0.1	14	9.8 ± 0.2	1.0 ± 0.3	0.1 ± 0.1	...
Median	–	–	33 per cent	–	1.2 ± 0.03	0.27 ± 0.02	12 ± 3	10.1 ± 0.2	2.4 ± 0.1	0.2 ± 0.1	−0.014 ± 0.009

of our galaxies correspond to SFRs (uncorrected for extinction) of $SFR^{obs}_{H\alpha}(M_\odot\ yr^{-1}) \approx 3$, 6 and 21 $M_\odot\ yr^{-1}$ at $z = 0.8$, 1.47 and 2.23, respectively. The median $E(B-V)$ for our sample is $E(B-V) = 0.2 \pm 0.1$ (see Table 1), which corresponds to $A_{H\alpha} = 0.79 \pm 0.16$ ($A_V = 0.96 \pm 0.20$). This suggests reddening corrected star formation rates of $SFR^{corr}_{H\alpha}(M_\odot\ yr^{-1}) \approx 6$, 13 and 43 $M_\odot\ yr^{-1}$ at $z = 0.8$, 1.47 and 2.23, respectively. Hereafter, we use an extinction value of $A_{H\alpha} = 1.0$ mag as used in previous works based on the HiZELS survey (e.g. Sobral et al. 2012; Ibar et al. 2013; Stott et al. 2013b, Thompson et al. 2017) in order to compare consistently.

2.5 Spatial extent

To measure the spatial extent of the galaxy, we calculate the half-light radii ($r_{1/2}$). Those are calculated from the collapsed continuum subtracted cubes, where the encircled Hα flux decays to half its total integrated value. The total integrated value is defined as the total Hα luminosity within a Petrosian radius. We adopted the 'Sloan Digital Sky Survey' Petrosian radius definition with $R_{P,\,lim} = 0.2$. We account for the ellipticity and position angle (PA) of the galaxy obtained from the best-fitting disc model (see Section 3). The $r_{1/2}$ errors are derived by bootstrapping via Monte Carlo simulations the errors in measured emission line intensity and estimated dynamical parameters of each galaxy. The half-light radii are corrected for beam-smearing effects by subtracting the seeing (0.15 arcsec) in quadrature. The median $r_{1/2}$ for our sample is found to be 2.4 ± 0.1 kpc (Table 1), which is consistent with previous studies at similar redshift range (Swinbank et al. 2012a).

2.6 Average ISM properties

To analyse the Hα and [N II] line fluxes for our targets, we first collapse each data cube into a one-dimensional spectrum (see Fig. 2). In eight cases, we detect the [N II] λ6583 emission line, deriving a median ratio of [N II]/Hα = 0.27 ± 0.02, with a range between 0.10 < [N II]/Hα < 0.43 (Table 1). None of the galaxies display strong active galactic nucleus (AGN) signatures in their rest-frame optical spectra (Fig. 2).

To search for fainter lines and obtain the mean properties of our observed sample we de-redshift each spectrum to rest-frame and co-add them (weighted by flux), yielding the composite spectrum shown in Fig. 2. Weighting by flux instead of signal-to-noise helps to smooth residual features seen in low S/N spectra (e.g. SA22-54, UDS-17 in Fig. 2). In this stacked spectrum, we measure a [N II]/Hα ratio of 0.25 ± 0.04 that is consistent with the median ratio derived for our sample. We also make a weak detection of the [S II]λλ6716, 6731 doublet and derive a flux ratio of $I_{6716}/I_{6731} = 1.04 \pm 0.31$. If we assume a typical H II region temperature of 10^4 K, then the measured I_{6716}/I_{6731} ratio corresponds to an electron density in the range of 100–1000 cm^{-3} (Osterbrock et al. 1989), and an upper limit to the ionized gas mass in the ISM of 4–40 × 10^{10} $M_\odot$ for a disc galaxy with half-light radius of ∼2.4 kpc (Table 1). For an isobaric density distribution of the ionized gas, the density is defined in terms of the mean ISM pressure P and mean electron temperature ($T_e \sim 10^4$ K), through $P/k_B \sim T_e\ n_e$. Therefore, we estimate a median ISM pressure of $P/k_B \sim 10^{6-7}$ K cm^{-3} that is ∼100–1000 times higher than the typical ISM pressure in the Milky Way (∼10^4 K cm^{-3}) and consistent with other high-z galaxy ISM pressure estimates (Swinbank et al. 2015). Although this value has considerable uncertainty, the derived pressure is compatible with hydrodynamic models that suggest that typical pressure in the ISM of star-forming galaxies should increase from ∼10^4 K cm^{-3} at $z = 0.1$ to ∼10^{6-7} K cm^{-3} at $z = 2$ (Crain et al. 2015). The I_{6716}/Hα flux ratio reflects the ionization strength of the ISM. We measure I_{6716}/Hα = 0.12 ± 0.03. Considering also the derived [N II]/Hα flux ratio, we suggest an ionization parameter of $\log_{10}(U\ cm^{-3}) = -3.6 \pm 0.3$ (Osterbrock et al. 1989; Collins & Rand 2001). Those median values are in agreement with Swinbank et al. (2012a), Stott et al. (2013a) and Sobral et al. (2013a, 2015).

2.7 Galaxy dynamics

To measure the dynamics of each galaxy, we fit the Hα and [N II] λλ6548, 6583 emission lines pixel-by-pixel. Following Swinbank et al. (2012a), we use a χ^2 minimization procedure, estimating the noise per spectral channel from an area that does not contain source emission. We first attempt to identify a Hα line in each 0.1 arcsec × 0.1 arcsec (∼1 ×1 kpc, which corresponds to the approximate PSF), although if the fit fails to detect the emission line, the area is increased by considering the neighbouring pixels, for example using the averaged signal from an area of 3×3 pixels. We use the criterion that the fit requires a S/N > 5 to detect the emission line in each pixel, and when this criterion is met then we simultaneously fit the Hα and [N II] λλ6548, 6583 emission allowing the centroid, intensity and width of the Gaussian profile to vary (the FWHM of the Hα and [N II] lines are coupled in the fit).

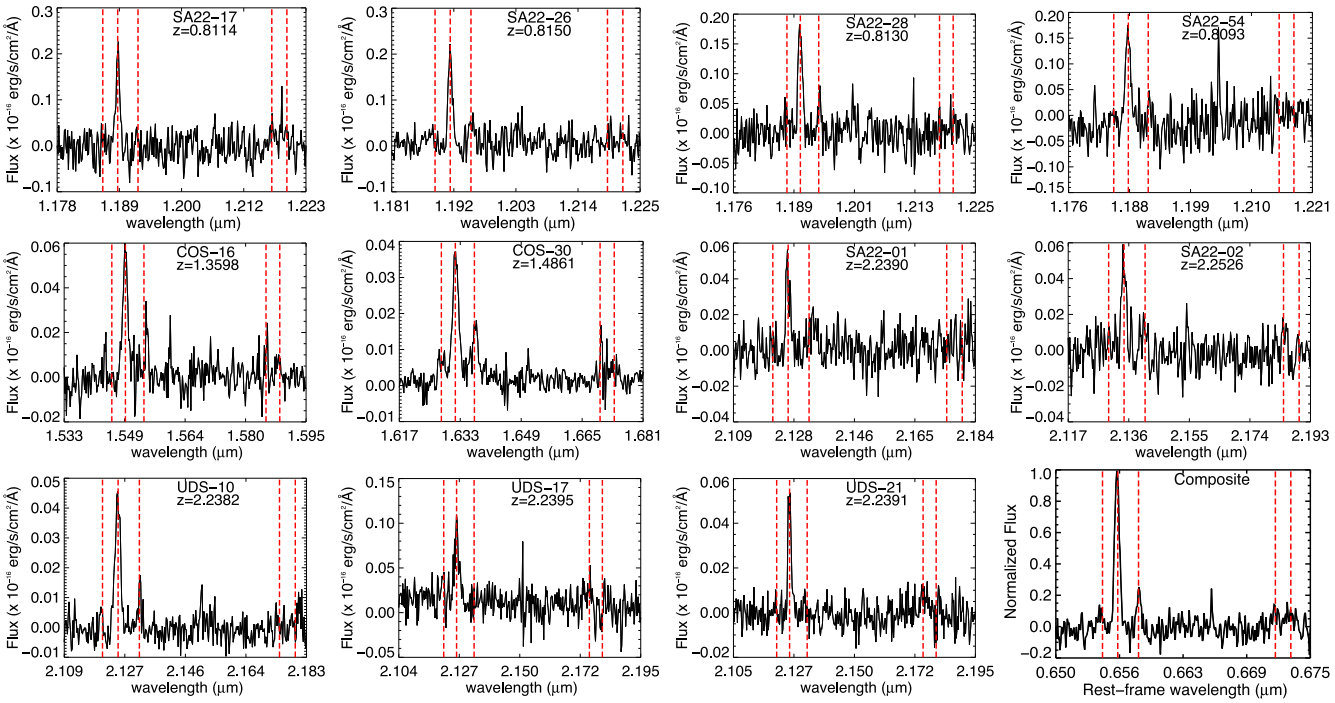

Figure 2. Spatially integrated one-dimensional spectra around the redshifted Hα emission for each of the galaxies in our sample. Hα, [N II]$\lambda\lambda$ 6583, 6548 and [S II] $\lambda\lambda$ 6716, 6731 emission lines are represented by the red-dashed lines. We detect [N II] emission in eight targets within our sample and the median [N II]/Hα for the sample is 0.27 ± 0.02, with a range of $0.10 <$ [N II]/Hα < 0.43. None of the galaxies display strong AGN signatures in their near-infrared spectra (e.g. broad lines or high [N II]/Hα ratios).

Even at $\sim$ kpc-scale resolution, there is a contribution to the line widths of each pixel from the large-scale velocity motions across the galaxy, which must be corrected for Davies et al. (2011). This is calculated for each pixel where the Hα emission is detected. We calculate the local luminosity-weighted velocity gradient (ΔV) across the PSF (ΔR) and subtract this from the measured velocity dispersion (see Stott et al. 2016, for more details). We show the Hα intensity, velocity and line of sight velocity dispersion maps in Fig. 3 for our sample.

3 ANALYSIS, RESULTS AND DISCUSSION

In Fig. 3, we can see a variety of Hα structures, including various levels of clumpiness of the emission within our sample. However, we note that resolution effects tend to smooth kinematic deviations making galaxy velocity fields appear more disky than they actually are (Bellocchi et al. 2012). Fig. 3 also shows that there are strong velocity gradients in many cases (e.g. SA22-28, SA22-54) with peak-to-peak differences [$V_{\rm max}$ sin(i)] ranging from 90 to 180 km s^{-1} and ratio of peak-to-peak difference to line-of-sight velocity dispersion (σ) of $V_{\rm max}$ sin(i)/$\sigma = 1.1$–3.8. This is in concordance with previous observations of galaxies at $z \sim 2$ (van Starkenburg et al. 2008; Law et al. 2009; Förster Schreiber et al. 2009; Gnerucci et al. 2011b; Genzel et al. 2011). Assuming that the dynamics of the underlying mass distribution are coupled to the measured kinematics of the ionized gas, then these observed high-z galaxies are consistent with highly turbulent systems.

Although a ratio of $V_{\rm max}/\sigma = 0.4$ has been used to crudely differentiate rotating systems from mergers (Förster Schreiber et al. 2009), more detailed kinematic modelling is essential to reliably distinguish these two populations. We therefore attempt to model the two-dimensional velocity field by first identifying the dynamical centre and the kinematic major axis. We follow Swinbank et al. (2012a) to construct two-dimensional models with an input rotation curve following an arctan function [$V(r)$=$\frac{2}{\pi} V_{\rm asym}$ arctan($r/r_{\rm t}$)], where $V_{\rm asym}$ is the asymptotic rotational velocity and $r_{\rm t}$ is the effective radius at which the rotation curve turns over (Courteau 1997). This model has six free parameters [$V_{\rm asym}$, $r_{\rm t}$, [x/y] centre, PA and disc inclination] and a genetic algorithm (Charbonneau 1995) is used to find the best fit (see Swinbank et al. 2012a for more details). The best-fitting kinematics maps and velocity residuals are shown in Fig. 3, the best-fitting inclination and disc rotation speeds are given in Table 2. The mean deviation from the best-fitting models within the sample (indicated by the typical RMS) is $\langle$data $-$ model$\rangle = 27 \pm 2$ km s^{-1} with a range of $\langle$data $-$ model$\rangle$ = 18–40 km s^{-1}. These offsets are probably the product of an un-relaxed dynamical component indicated by the high mean velocity dispersion $\sigma = 71 \pm 1$ km s^{-1} of our sample (Table 2), dynamical substructures or effects of gravitational instability within the disc.

We use the dynamical centre and PA derived from the best-fitting dynamical model to extract the one-dimensional rotation curve across the major kinematic axis of each galaxy (see Fig. 3). Three targets (SA22-26, SA22-54 and SA22-02) do not show a flattening of the velocity curve at large radii, so $V_{\rm asym}$ can only be estimated using an extrapolation of the true rotational velocity for these targets.

In order to distinguish between rotation and motion from disturbed kinematics, we use 'kinemetry' that measures the asymmetry of the velocity field and line-of-sight velocity dispersion maps for each galaxy (Shapiro et al. 2008). This technique has been well calibrated and tested at low redshift (e.g. Krajnović et al. 2006), whereas at high redshift it has been used to determine the strength of deviations of the observed velocity and dispersion maps from an ideal

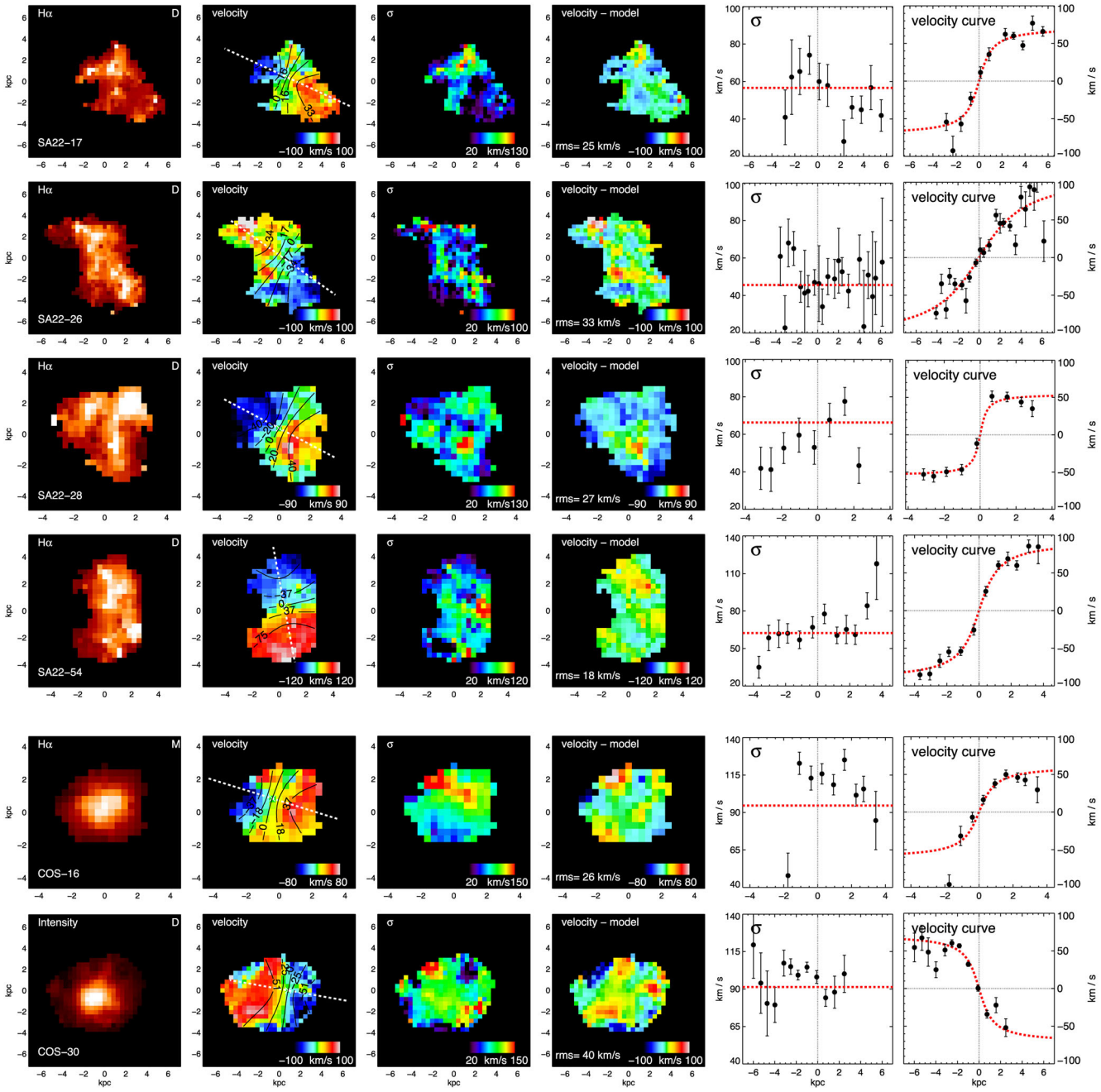

Figure 3. Hα intensity, velocity, line-of-sight velocity dispersion (σ), residual fields, one-dimensional velocity dispersion profile and one-dimensional velocity profile (columns) for 11 galaxies from our observed sample (rows). The Hα intensity map also shows the classification done by kinemetry analysis (see Section 3): six galaxies were classified as discs (D), four as mergers (M) and one as unresolved/compact (C). The unresolved/compact source (SA22-01) has no modelling. The velocity field has overplotted the kinematical centre, the mayor kinematic axis and velocity contours of the best-fitting two-dimensional kinematical disc model. The line-of-sight velocity dispersion (σ) field is corrected for the local velocity gradient ($\Delta V/\Delta R$) across the PSF. The residual map is constructed by subtracting the best-fitting kinematic model from the velocity map: the root mean square (r.m.s.) of these residuals are given in each panel. The one-dimensional velocity profiles are derived from the two-dimensional velocity field using the best-fitting kinematical parameters and a slit width of $\sim$1 kpc across the major kinematic axis. The error bars show the 1σ uncertainty. In the velocity dispersion profile plots, the red-dashed line shows the mean galactic velocity dispersion value. The dotted grey line represents the best-fitting dynamical centre (Table 2). In the last column, the red-dashed line shows the best one-dimensional fit using an arctan model for each source. The dotted vertical and horizontal grey lines represent the best-fitting dynamical centre and the zero velocity point, respectively.

rotating disc (Shapiro et al. 2008; Alaghband-Zadeh et al. 2012; Swinbank et al. 2012a; Sobral et al. 2013a). Briefly, kinemetry proceeds to analyse the two-dimensional velocity and velocity dispersion maps using azimuthal kinematic profiles in an outward series of best-fitting elliptical rings. The kinematic profile as a function of angle is then expanded harmonically, which is equivalent to a Fourier transformation that has coefficients k_n at each tilted ring (see Krajnović et al. 2006 for more details).

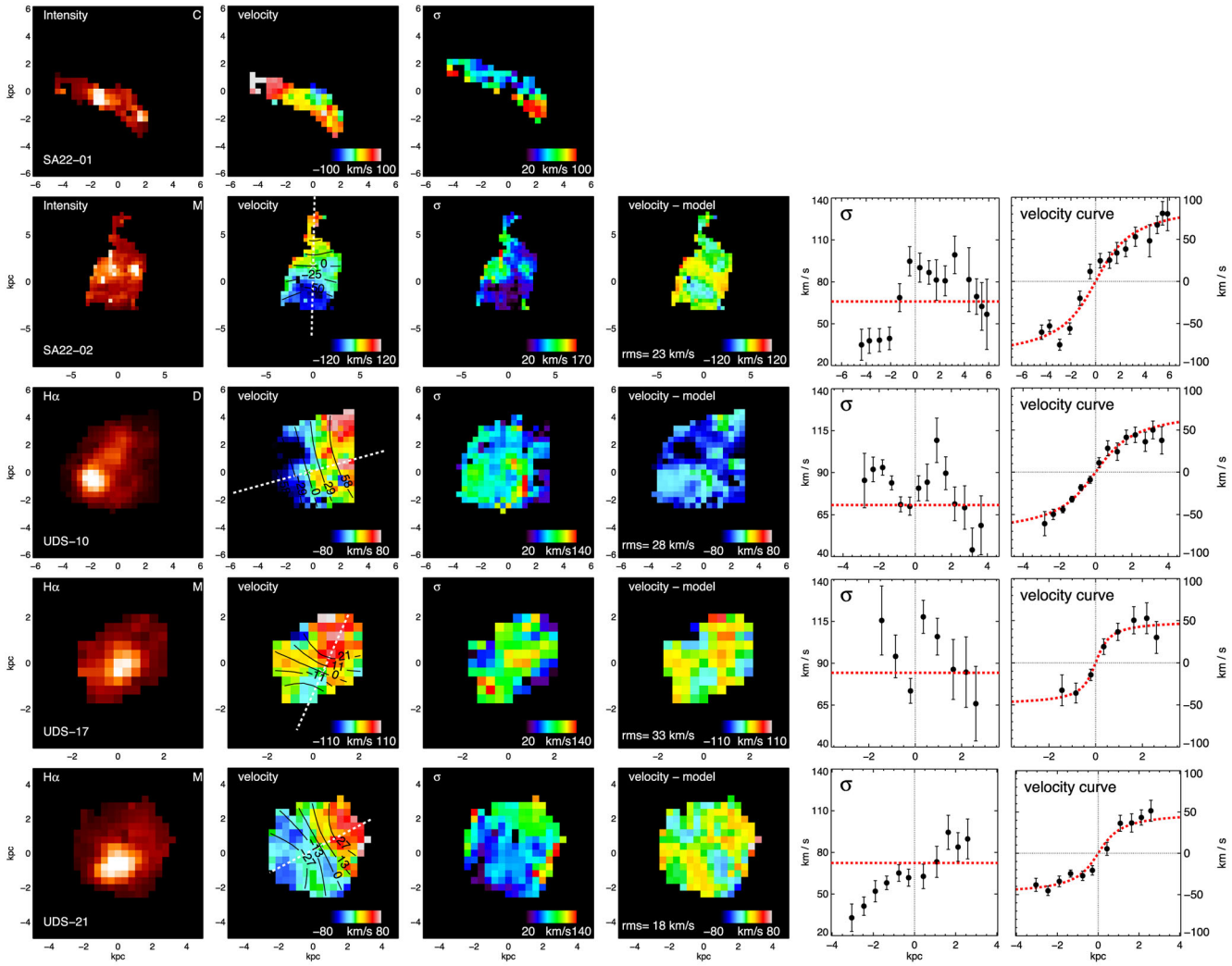

Figure 3 – *continued*

Table 2. Dynamical properties of the galaxies in our sample. 'inc.' is the inclination angle defined by the angle between the line of sight and the plane of the galaxy disc (for a face-on galaxy, inc = 0°). σ is the average velocity dispersion across the galaxy image corrected for 'beam-smearing' effects due to PSF; see Section 2.7. $V_{\rm asym}$ and $V_{2.2}$ are inclination corrected. The χ^2_ν of the best two-dimensional fit for each source is given in column six. $K_{\rm Tot}$ is the kinemetry coefficient. The classes in the final column denote Disc (D), Merger (M) and Compact (C) (see Section 3 for more details of these parameters).

ID	inc. (deg)	σ (km s^{-1})	$V_{\rm asym}$ (km s^{-1})	$V_{2.2}$ (km s^{-1})	χ^2_ν	$K_{\rm Tot}$	Class
SA22-17	72	57 ± 13	75 ± 2	62 ± 4	1.1	0.36 ± 0.04	D
SA22-26	53	46 ± 11	142 ± 3	120 ± 12	1.5	0.24 ± 0.03	D
SA22-28	65	66 ± 8	60 ± 3	52 ± 7	1.7	0.22 ± 0.03	D
SA22-54	63	62 ± 10	104 ± 2	95 ± 5	1.3	0.14 ± 0.02	D
COS-16	53	95 ± 8	77 ± 11	59 ± 10	1.9	0.99 ± 0.09	M
COS-30	63	91 ± 13	81 ± 3	61 ± 3	2.9	0.16 ± 0.02	D
SA22-01	–	–	–	–	–	–	C
SA22-02	71	66 ± 9	100 ± 3	85 ± 12	2.0	0.81 ± 0.09	M
UDS-10	32	71 ± 10	143 ± 10	85 ± 7	3.2	0.24 ± 0.04	D
UDS-17	71	84 ± 14	53 ± 6	40 ± 7	9.0	0.90 ± 0.08	M
UDS-21	40	72 ± 11	78 ± 14	58 ± 12	1.6	0.75 ± 0.07	M
Mean	58	71 ± 3	91 ± 2	72 ± 3	2.6	0.48 ± 0.02	...

Defining the velocity asymmetry (K_V) and the velocity dispersion asymmetry (K_σ) using the eigen k_n coefficients from the velocity and velocity dispersion maps, respectively, we measure the level of asymmetries from an ideal disc in our galaxies (we omit SA22-01 from this analysis as it is not well resolved). For an ideal disc, the values K_V and K_σ will be zero. In a merging system, strong deviations from the idealized case produces large K_V and K_σ values. The total asymmetry is defined as $K^2_{\rm Tot} = K^2_V + K^2_\sigma$ and we use this quantity to differentiate discs ($K_{\rm Tot} < 0.5$) from mergers ($K_{\rm Tot} > 0.5$) following Shapiro et al. (2008). The $K_{\rm Tot}$ errors are derived by bootstrapping via Monte Carlo simulations the errors in measured velocities, velocity dispersions and estimated dynamical parameters of each galaxy.

Bellocchi et al. (2012) proposed a modified kinemetry criterion ($K_{\rm Tot,\,B12}$), which try to distinguish between post-coalescence mergers and discs. As the major merger evolves, the central region tends to relax rapidly into a disc meanwhile the outer parts remain out of equilibrium. Therefore, the outer regions retain better the memory of a merger event (Kronberger et al. 2007). In order to consider this effect, Bellocchi et al. (2012) weights more highly the outskirts of each galaxy when combining the asymmetries measured from the velocity and velocity dispersion maps.

These two kinemetry criteria have been compared with a visual classification scheme done at higher spatial resolution. Hung et al. (2015) observed 18 (U)LIRGs at $z < 0.088$ with the *Hubble Space Telescope* (*HST*) Advanced Camera for Surveys and considered another six sources from the Digitized Sky Survey. They classified galaxies by inspecting their optical morphologies (Larson et al. 2016) and then they obtained IFS data for this sample from the Wide-Field Spectrograph. They artificially redshifted their local IFS observations to $z = 1.5$ to make a comparison with IFU seeing-limited observations (0.5 arcsec) at high-z. Hung et al. (2015) concluded that Shapiro et al. (2008)'s kinemetry criterion ($K_{\rm Tot}$) tends to underestimate the merger fraction whereas Bellocchi et al. (2012)'s kinemetry criterion ($K_{\rm Tot,\,B12}$) overestimated the number of mergers within the same sample. Hereafter, we will use the kinemetry criterion defined by Shapiro et al. (2008) to classify our targets, considering that our merger fraction values are likely to be lower limits at each redshift.

From the kinemetry criterion, we classify four targets as merger systems and six targets as rotating systems (see Table 2). In addition, from the kinemetry criterion error rate (see Shapiro et al. 2008, for more details), we expect that ∼1 merger is being misclassified as a disc and ∼1 disc is being misclassified as merger. The fraction of rotating systems within our sample is ∼60 per cent, which is consistent within 1σ with that found from other Hα IFU surveys at similar high redshift (e.g. Förster Schreiber et al. 2009; Jones et al. 2010b; Wisnioski et al. 2011; Swinbank et al. 2012a). We note that most of our mergers are identified in galaxies at $z \sim 2.23$ and the large error estimates are inherent of the low statistics of our sample.

In Fig. 4, we plot the $K_{\rm Tot}$ parameter against the $V_{\rm max}/\sigma$ ratio for our sample and that presented by Swinbank et al. (2012a). All of these galaxies were observed at ∼kpc-scale resolution using AO. We find no correlation between both quantities. Although galaxies classified as mergers by kinemetry tend to lie in the region with lower $V_{\rm max}/\sigma$ ratio, we find that the $V_{\rm max}/\sigma = 0.4$ merger criterion is not consistent with the more sophisticated kinematic estimate $K_{\rm Tot}$, suggesting that the former criterion underestimates the total number of mergers within a given galaxy sample. This also suggests that a detailed kinematic analysis is needed in order to classify mergers from galaxy discs.

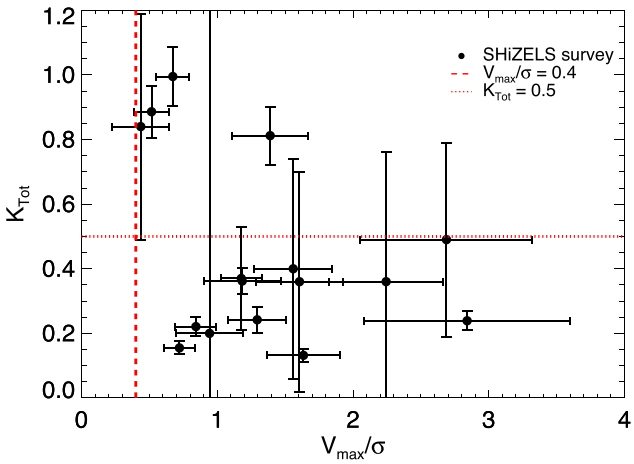

Figure 4. The kinematic measure $K_{\rm Tot}$ (see Section 3) against the $V_{\rm max}/\sigma$ ratio for the SHiZELS survey. The red-dashed line shows the $V_{\rm max}/\sigma = 0.4$ ratio that has been used to crudely differentiate rotating systems from mergers (Förster Schreiber et al. 2009). The red-dotted line shows the $K_{\rm Tot} = 0.5$ value that is used to distinguish between galaxy discs from mergers (Shapiro et al. 2008). Although there is no strong correlation between both quantities, it is notable that galaxies classified as mergers by kinemetry criterion tend to show lower $V_{\rm max}/\sigma$ ratio, however not as low as 0.4. This suggests that the $V_{\rm max}/\sigma = 0.4$ criterion tends to underestimate the total number of mergers in a given galaxy sample.

Hereafter, we will refer to the 'SHiZELS' survey as the compilation of the observations presented in this work with the previous observations by Swinbank et al. (2012a). In this previous campaign they observed nine Hα-selected star-forming galaxies between $z = 0.84$–2.23 with SINFONI. This sample was also drawn from the HiZELS survey. The median $M_\star$ and SFR are $\sim 2 \times 10^{10}$ M$_\odot$ and ∼7 M$_\odot$ yr^{-1}, respectively (see Swinbank et al. 2012a, for more details).

3.1 The stellar-mass Tully–Fisher and $M_\star$–$S_{0.5}$ relations

The TFR is a fundamental scaling relation describing the interdependence of luminosity or stellar mass and the maximum rotational velocities (a dark matter mass tracer) in galaxies. It allows us to trace the evolution of the mass-to-luminosity ratio of populations of galaxies at different epochs. Recently, the KROSS (Stott et al. 2016; Tiley et al. 2016; Harrison et al. 2017) has provided a new perspective on TFR evolution by observing ∼600 galaxies at $z \sim 0.9$. Tiley et al. (2016) derived an evolution of the stellar-mass TFR zero-point of -0.41 ± 0.08 dex for rotationally supported galaxies defined with $V/\sigma > 3$. However, when they analysed their data without this V/σ constraint, they did not find any significant evolution of the $M_\star$–TFR zero-point. We note that the $M_\star$–TFR zero-point evolution found by Tiley et al. (2016) is contrary to some previous studies conducted at similar redshift (Miller et al. 2011, 2012; Di Teodoro et al. 2016).

Similarly, Weiner et al. (2006a) and Kassin et al. (2007) introduced the kinematic measure $S_{0.5} = (0.5V^2 + \sigma^2)^{0.5}$ that considers support by both rotational motions and dispersion arising from disordered motions (Weiner et al. 2006a). Kassin et al. (2007) computed the $M_\star$–TFR and $M_\star$–$S_{0.5}$ relations within 544 galaxies at $0.1 < z < 1.2$. The $M_\star$–$S_{0.5}$ relationship was found to be a tighter

relation compared with the $M_\star$–TFR relation, and this relation also showed no evolution with redshift in either intercept or slope.

When measuring circular velocities, to be consistent with the previous Swinbank et al. (2012a) campaign, we use velocities observed at 2.2 times the disc scalelength ($V_{2.2}$) corrected for inclination effects. The disc scalelength (r_d) is defined as the radius at which the galaxy Hα intensity has decreased to e^{-1}(∼0.37) times its central value.

3.1.1 *The Stellar mass Tully–Fisher relation*

In Fig. 5, we study the $M_\star$–TFR at $z = 0.8$–2.23 using SHiZELS survey galaxies classified as disky by our kinemetry analysis. The stellar masses and velocities from the comparison samples have been estimated in a fully consistent way, and these values (or corrections, where necessary) are presented in Swinbank et al. (2012a). We also show the TF relations at $z = 0$ (Pizagno et al. 2005) and the best-fitting relation at $z = 1$–2 (Swinbank et al. 2012a) from the literature. Even though we do not attempt to fit a relation to our data, we can see from Fig. 5 that apparently our sample is consistent with no evolution in the zero-point of the $M_\star$–TFR out to $z = 0.8$–2.23.

As suggested by Tiley et al. (2016), we estimated the rotational velocity to dispersion velocity ratio. This is done by calculating the $V_{2.2}/\sigma$ ratio. We show this parameter colour-coded in Fig. 5. We find that galaxies with lower $V_{2.2}/\sigma$ ratio (i.e. with greater pressure support) tend to be scattered to lower values along the rotational velocity axis: this is consistent with Tiley et al. (2016), who found an evolution of the zero-point TFR at $z = 0.9$ when they select galaxies with $V_{80}/\sigma \geq 3$ within their sample (V_{80} is the velocity observed at the radius that encloses the 80 per cent of the total Hα intensity of the galaxy), although the complete sample is consistent with no evolution in the TFR zero-point.

This result suggests that the large scatter measured from the $M_\star$–TFR at high-z may be produced by galaxies that are supported by a combination of rotational and disordered motions. If we do not take into account this effect then this could produce misleading conclusions. We note that galaxies that have greater rotational support within the SHiZELS survey tend to lie closer to the $M_\star$–TFR at $z = 2$ derived by Swinbank et al. (2012a), whilst galaxies with strong disordered motion support tend to be have a greater offset from this relationship. This trend perhaps implies that galaxies may be moving on to the $M_\star$–TFR with time as the dynamics of the stars and gas in the central few kpc of the haloes are yet to relax into a disc-like system.

3.1.2 *The $M_\star$–$S_{0.5}$ relation*

The stellar mass TFR is found to be sensitive to which process dominates the support of the galaxy. The scatter increases when galaxies with pressure support equivalent to the rotational support ($V/\sigma \sim 1$) are included. Perhaps a more fundamental relation is the $M_\star$–$S_{0.5}$ relationship (Weiner et al. 2006a; Kassin et al. 2007) that considers the support given by ordered and disordered motions within the galaxy. In Fig. 5, we show the $M_\star$–$S_{0.5}$ relation for the SHiZELS survey using the inclination-corrected speeds, colour-coded by V/σ ratio. We also show the $z \sim 0.2$ $M_\star$–$S_{0.5}$ relationship from Kassin et al. (2007) and the best linear fit to the SHiZELS survey sample. We note that this relationship is fitted in the form $\log_{10}(S_{0.5}) = a + b \log_{10}(M_\star \times 10^{-10}\ \mathrm{M}_\odot)$, where '$a$' is the interceptor. From Fig. 5, it can be seen that our sample agrees with the $z \sim 0.2$ $M_\star$–$S_{0.5}$ relationship within 1σ uncertainty: this is consistent with either no

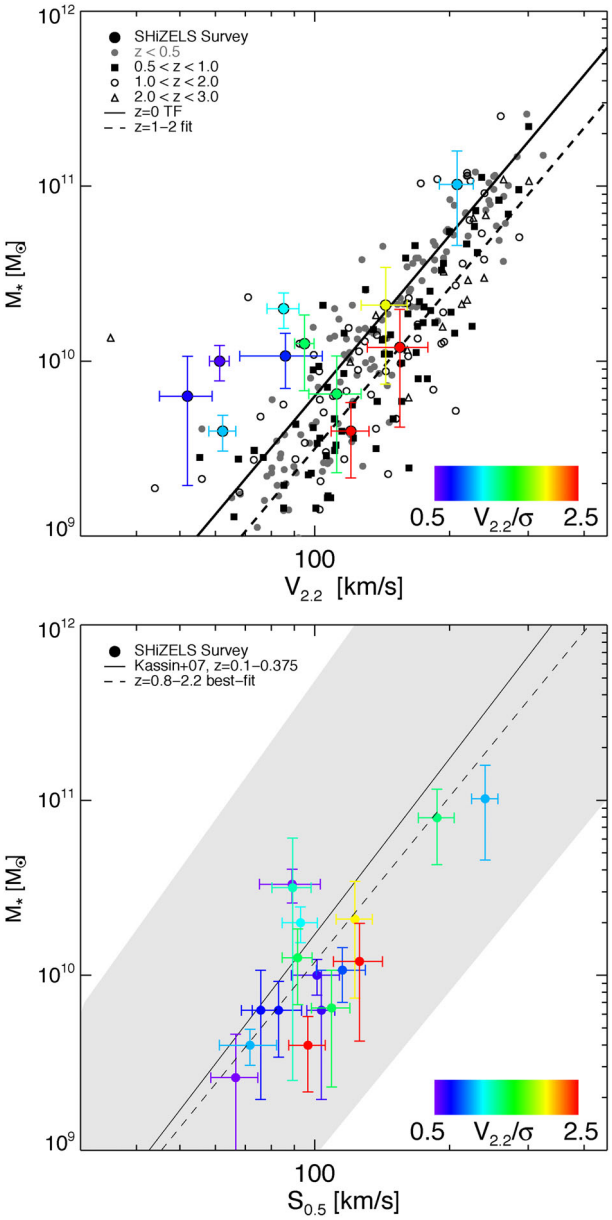

Figure 5. *Top*: Evolution of the stellar mass TF relation measured from the SHiZELS survey at $z = 0.8$–2.23 colour-coded using the $V_{2.2}/\sigma$ ratio. We only show our galaxies consistent with rotating systems together with their 1σ velocity and stellar mass uncertainties. The solid line denotes the TFR at $z = 0$ from Pizagno et al. (2005). The dashed line represents the best-fitting TF relation at $z = 1$–2 from Swinbank et al. (2012a) based on the compilation of high-redshift points from Miller et al. (2011, 2012, $z = 0.6 - 1.3$); Swinbank et al. (2006, $z = 1$); Swinbank et al. (2012a, $z = 1.5$); Jones et al. (2010b, $z = 2$); Cresci et al. (2009, $z = 2$) and Gnerucci et al. (2011b, $z = 3$). Galaxies with lower relative rotational support tend to be scattered to lower values along the velocity axis. This is consistent with the result found by Tiley et al. (2016). *Bottom*: The $M_\star$–$S_{0.5}$ relationship measured from the SHiZELS survey at $z = 0.8$–2.23. The error bars show the 1σ stellar mass and $S_{0.5}$ uncertainties. The data is colour-coded as in the image above. The solid line represents the relation at $z \sim 0.2$ from Kassin et al. (2007) and the shaded area represents its 1σ uncertainty. The dashed line corresponds to the best-linear-fit to our data. Our scatter is tighter than the intrinsic $M_\star$–$S_{0.5}$ scatter. The slope (0.32 ± 0.2) and the intercept at 10^{10} $\mathrm{M}_\odot$(1.98 ± 0.09) found from our best fit are consistent with the uncertainties of the $z \sim 0.2$ relation. This is consistent with no evolution of the $M_\star$–$S_{0.5}$ relation with redshift up to $z = 2.23$.

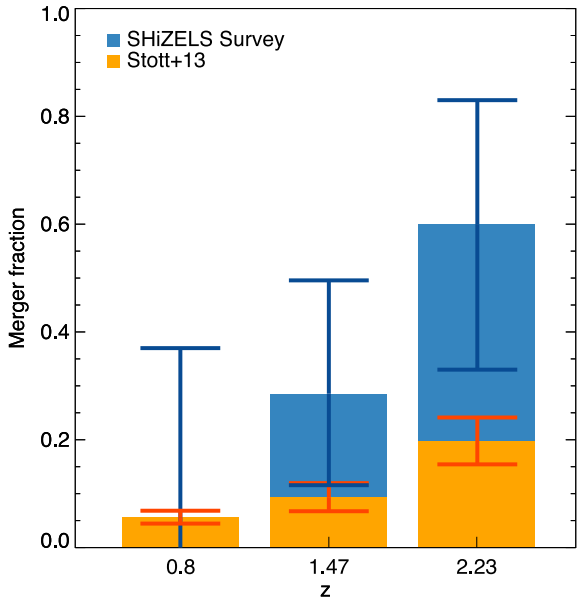

Figure 6. In blue are represented the kinematically selected mayor merger fractions measured from the SHiZELS survey at $z = 0.8$–2.23. The error bars for the SHiZELS survey are estimated by assuming binomial statistics (see Section 3). The orange colour corresponds to the data at similar sSFR ($\sim 10^{-9}$ yr^{-1}) from Stott et al. (2013a), who use the M_{20} morphological criterion to classify mergers. We find higher merger fraction at each redshift slice.

evolution of interceptor or slope of the $M_\star$–$S_{0.5}$ relation with redshift (Kassin et al. 2007). Despite the low number statistics, we do not identify any dependence on V/σ for this relation, contrasting with what was previously seen in the $M_\star$–TFR (Fig. 5).

This relationship is consistent with a scenario of galaxy formation that begins with matter assembling into a dark-matter halo with turbulent kinematics. The baryonic component forms protodiscs that are initially supported by a combination of rotational and disordered motions. Finally, the material in these protodiscs settles down, unless they undergo major mergers (Kassin et al. 2007).

3.2 Merger fraction

To test whether it is galaxy mergers, secular processes or a combination of both that dominate and drive galaxy evolution at the peak era for star formation, we need to measure the merger fraction ($f_{\rm merg}$) at this epoch. From a theoretical perspective in the ΛCDM paradigm, dark matter haloes merge hierarchically from the bottom up (e.g. Lacey & Cole 1993; Cole et al. 2000; Springel et al. 2005). As baryonic matter traces the underlying dark matter, we expect that galaxies merge hierarchically as well.

Stott et al. (2013a) noted that the typical sSFR for galaxies increases with redshift within the HiZELS sample. They found greater merger fractions with increasing sSFR suggesting that major mergers can lead to galaxies having unusually high sSFR. Although the targets within the SHiZELS survey have higher SFR at higher redshift, they also have higher stellar masses, maintaining the median sSFR per redshift slice roughly constant (see Fig. 1).

We define 'merger fraction' as the number of galaxies classified as merger by the kinemetry criterion (see Section 3) divided by the total number of galaxies in the redshift slice (we do not consider the unresolved galaxy classified as 'compact' in this analysis).

In Fig. 6, we show the variation of the merger fraction as a function redshift for the $z = 0.8$, 1.47 and 2.23 redshift slices. From the SHiZELS survey, we find a merger fraction of $0.0^{+0.4}$, $0.3^{+0.2}_{-0.2}$ and $0.6^{+0.2}_{-0.3}$ at $z = 0.8$, 1.47 and 2.23, respectively. The error in the merger fraction were estimated by assuming binomial statistics. These values are consistent with previous IFU surveys (e.g. Shapiro et al. 2008; Förster Schreiber et al. 2009).

We compare with Stott et al. (2013a) who used the M_{20} morphological classification (Lotz, Primack & Madau 2004) in the HiZELS sample but we only consider the merger fraction calculated for those galaxies with similar sSFR values ($\sim 10^{-9}$ yr^{-1}). From Fig. 6, we find a clear increase in merger fraction from $z = 0.8$ to $z = 2.23$ that seems to be stronger than the increase found by Stott et al. (2013a). This suggests that methods based on surface brightness morphology classification may underestimate the number of major mergers at low sSFR and similar (0.2–0.7 arcsec) spatial resolution. We conclude that galaxy mergers may have a dominant role in the evolution of 'typical' star-forming galaxies at $z \geq 1.5$, but we caution regarding the low number of statistics.

3.3 Metallicity content

Measuring the internal enrichment and radial abundance gradients of high redshift star-forming galaxies provides a tool for studying the gas accretion and mass assembly process such as the gas exchange with the intergalactic medium. The [N II]/Hα emission line ratio can be used to determine the metallicity of high-z galaxies using the conversion $12 + \log_{10}({\rm O/H}) = 8.9 + 0.57 \log_{10}([{\rm N\,II}]/{\rm H}\alpha)$ (Pettini & Pagel 2004). Our sample has a median metallicity of $12 + \log_{10}({\rm O/H}) = 8.57 \pm 0.05$, which is slightly below but still consistent with the solar value. Also our galaxies have metallicities consistent with previous studies that derive typical metallicities of 8.66 ± 0.05 and 8.58 ± 0.07 for Hα-selected samples at $z \sim 0.81$ and $z \sim 0.84$–2.23, respectively (Queyrel et al. 2012; Swinbank et al. 2012a; Sobral et al. 2013a).

A relationship between mass, metallicity and SFR has been found in both the local and high-z Universe (Mannucci et al. 2010; Lara-López et al. 2010, 2013) and measured by Stott et al. (2013b) for a sample drawn from the HiZELS survey at $z \sim 1$. The shape of this 'fundamental metallicity relationship' (FMR) is, to first order, a manifestation of the positive correlation of the metallicity and stellar mass at fixed SFR and a negative correlation of the metallicity and SFR at fixed stellar mass. The shape of the FMR can be explained as the result of the competing effects of chemical enrichment of the gas by the evolving stellar population, star formation driven winds and the inflow of gas from the IGM. We test this relationship and its dependence on galaxy morphology using the SHiZELS survey. In Fig. 7, we show the difference between the measured metallicity of the SHiZELS survey and the metallicity predicted by the FMR at $z = 0.84$–1.47 (Stott et al. 2013b). The measured scatter is consistent within 1σ uncertainties from the FMR. On average, we find that the metallicity content in our star-forming galaxies is similar to galaxies of similar mass and SFR at $z \sim 0.1$ (Stott et al. 2013b). We note that this suggests no evolution in the FMR up to $z \sim 2.23$. Although most of our galaxies at $z \sim 2.23$ are classified as mergers, we find no trend between mergers and discs morphologies within the residuals from this relationship.

In order to derive the chemical abundance gradients in our sample, we use the disc inclination and PA (derived from the best-fitting dynamical model) to define ∼1 kpc annuli centred at the dynamical centre. Within each annulus, we stack the spectrum (considering emission line offsets in each annulus) to measure the average [N II]/Hα flux ratio by fitting a double Gaussian profile with coupled Gaussian widths. For a detection, we enforce S/N > 5 thresholds

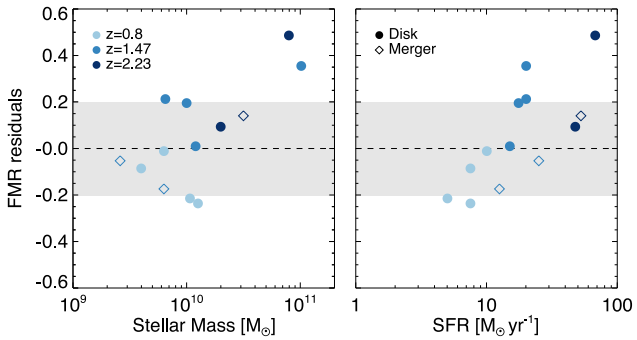

Figure 7. The metallicity residuals within the SHiZELS survey calculated as the subtraction between the measured metallicities and the metallicities predicted by the FMR of Stott et al. (2013b). We plot against the stellar mass (left) and SFR (right). Negative values mean metallicities lower than expected by the FMR. The sky blue, blue and dark blue colours represent the sources at $z = 0.8$, 1.47 and 2.23, respectively. Diamonds and circles show targets classified as Merger and Discs respectively from kinemetry criterion (see Section 3). The shaded area corresponds to the scatter of the FMR of 0.2 dex (Stott et al. 2013b). The measured residuals expected from the FMR is 0.23 dex, which is consistent with the relationship. We find no trend between galaxy morphology and metallicity content within our sample.

at each radius and a minimum of three radial detections per target. Then we fit a straight line as a function of galaxy radius in each case. From the eight galaxies with measured [N II]/Hα flux ratio detected from their one-dimensional spectra (see Section 2.6), five galaxies present reliable [N II]/Hα gradients. We show this in Fig. 8 and the individual metallicity gradients values are reported in Table 1. We find a median of $\Delta\log_{10}(\mathrm{O/H})/\Delta R = -0.014 \pm 0.009$ dex kpc^{-1}, i.e. a median gradient consistent with a negative gradient. In comparison, Swinbank et al. (2012a) found a slightly steeper median metallicity gradient ($\Delta\log_{10}(\mathrm{O/H})/\Delta R = -0.027 \pm 0.006$ dex kpc^{-1}) from their sample at similar redshift range. Considering the combination of both studies (the full SHiZELS sample), we find a median metallicity gradient of $\Delta\log_{10}(\mathrm{O/H})/\Delta R = -0.026 \pm 0.008$ dex kpc^{-1}. This result suggests that either low-metallicity gas from the halo or IGM is accreted on to the outer disc, or metal enrichment is higher in the central region of the galaxy.

We do not have simultaneous access to [O III] 5007, Hβ, Hα, and [N II] 6583 or [S II] 6717, 6731 emission lines to distinguish any possible strong AGN contribution within our sample via a BPT diagram (Baldwin, Phillips & Terlevich 1981). Considering $\log_{10}$([N II]/Hα) ≈ -0.2 flux ratio as a rough limit for identifying an AGN at $z \geq 0.8$ (Kewley et al. 2013), only the central kpc of SA22-26 might be affected by low AGN contamination. This conclusion is also supported by the lack of broad recombination lines in the spectra.

Just one galaxy (COS-16) shows a positive metallicity gradient within the SHiZELS survey – a system that is also classified as a major merger by the kinemetry criterion. From cosmological simulations, Tissera et al. (2016) found that galaxies with positive metallicity gradients tend to exhibit morphological perturbations and close neighbours. They suggest that those galaxies have a high probability of interactions/mergers due to a high number of surrounding satellites. They analyse the evolution of a gas-rich equal-mass merger and they found that both negative and positive metallicity gradients might be produced during different stages of the merger evolution.

We note that we do not find any clear correlation between the asymmetries measured from the kinemetry coefficients (K_V, K_σ and K_{Tot}) and the metallicity gradients observed within the SHiZELS survey.

3.4 Spatially resolved chemical abundances

A tentative anticorrelation between the metallicity gradient and the global integrated metallicity was previously hinted at the 'Mass Assembly Survey with SINFONI in VVDS' (MASSIV), using star-forming galaxies at $z \sim 1.2$ (Queyrel et al. 2012). They suggest that metallicity gradients are more frequently negative in metal-rich galaxies and more frequently positive in low-metallicity galaxies. In Fig. 9, we show the anticorrelation suggested by Queyrel et al. (2012), adding our SHiZELS galaxies and the sample observed by Stott et al. (2014). We calculate the average and median values per $\Delta\log_{10} = 0.1$ bin. Then we calculate the best linear fit to the average and median values. The slope is 2.5σ from being flat (2.0σ by fitting the median values), but due to beam-smearing effects and inclination angles the measured metallicity gradients are likely to be underestimated, especially those of Stott et al. (2014) and MASSIV samples that were measured on seeing-limited conditions ($\sim$0.7 arcsec). Stott et al. (2014) estimated that their observed metallicity gradients reflect only $\sim$70 per cent of the true values. This suggests that if we alleviate inclination angle effects with higher resolution IFU observations, these results will not change. Our results support the previous suggestion by Queyrel et al. (2012).

We note that positive metallicity gradients could be explained by the infall of metal-poor gas from the IGM into the centre of the galaxy, diluting the gas and lowering its metallicity in the central regions. If the funnelling of metal-poor gas into the centres of galaxies is triggered by galaxy mergers, then from the merger fraction

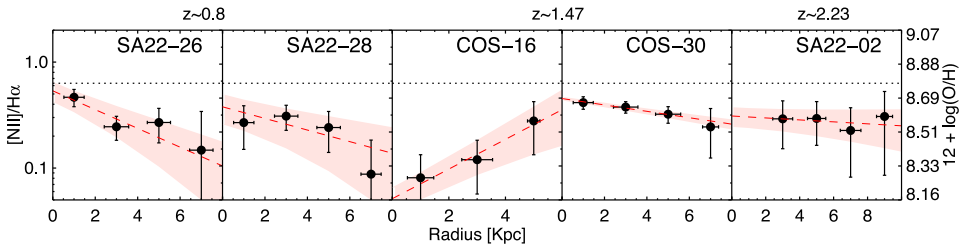

Figure 8. Metallicity gradients for five galaxies in our observed sample (Table 1) from spatially resolved measurements as function of the physical radius derived from the best kinematical model. The red dashed line represents the best linear fit and the shaded region represents 1-dex uncertainties. The dotted line shows the AGN limit of $\log_{10}$([N II]/Hα) ≈ -0.2 at $z = 0.8$ (Kewley et al. 2013). This suggests the potential for a starting AGN activity within the central kpc in source SA22-26. Within our sample, SA22-02 has a gradient consistent with zero; SA22-26, SA22-28 and COS-30 have negative gradients and COS-16 source has positive metallicity gradient.

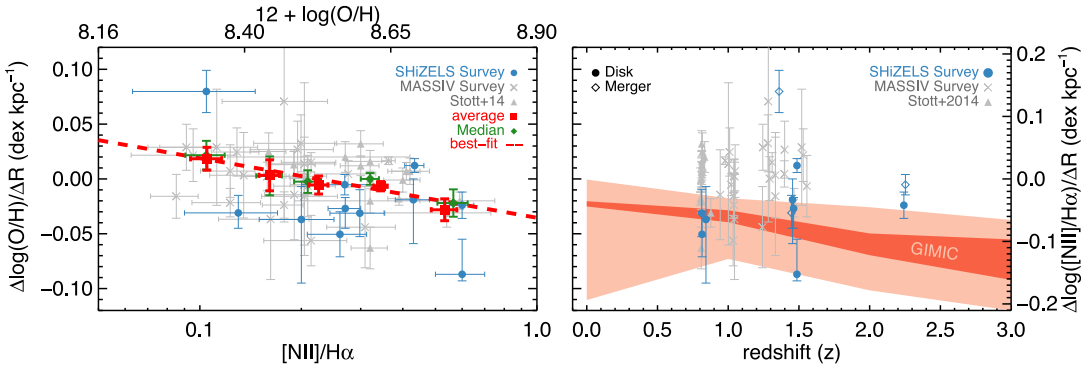

Figure 9. *Left*: Metallicity gradient as a function of the [N II]/Hα emission line ratio from the one-dimensional spectra of each galaxy. The sky blue circles are individual galaxies within the SHiZELS survey. The grey crosses denote the sample from the MASSIV survey (Queyrel et al. 2012) corrected for a Pettini & Pagel (2004) metallicity calibration. The grey triangles denote the sample from Stott et al. (2014). The red squares and green diamonds show the average and median metallicity content and metallicity gradient per $\Delta\log_{10}(\mathrm{O/H}) = 0.1$ bin, respectively. The error bars show 1σ uncertainties. Within the literature, we only consider [N II]/Hα fluxes ratio above 1σ detection threshold. The red-dashed line shows the best linear fit ($\Delta\log_{10}(\mathrm{O/H})/\Delta R = a + b \times \log_{10}(\mathrm{O/H})$) to the average values with a slope value of $a = -0.10 \pm 0.04$ and zero-point of $b = 0.89 \pm 0.30$. The SHiZELS survey supports the anticorrelation such that metallicity gradients tend to be negative in metal-rich galaxies and positive in low-metallicity galaxies (see also Queyrel et al. 2012). *Right*: Metallicity gradient as a function of redshift. We also show the theoretical evolution of the metallicity gradient with redshift from the GIMIC simulation (Crain et al. 2009; McCarthy et al. 2012). The shaded-red area shows the range of metallicity gradients for all disc galaxies in the simulation in the mass range $9.5 < \log_{10}(M/\mathrm{M}_{\odot}) < 11.5$, whilst the shaded light-red denotes the 1σ scatter at each epoch. Diamonds and circles show targets classified as Merger and Disc, respectively from kinemetry criterion (see Section 3). The metallicity gradients measured from the SHiZELS survey do not support the evolution predicted from the GIMIC simulation from $z = 0$ to $z = 1.47$.

estimated for the SHiZELS survey (Fig. 6), we should expect to find more systems with positive/flat metallicity gradients at $z \sim 2$.

Taking into account the metallicity gradients measured from the SHiZELS survey (Fig. 9), we compare its evolution with redshift with the prediction from the 'Galaxies-Intergalactic Medium Interaction Calculation' simulation (GIMIC; Crain et al. 2009; McCarthy et al. 2012), where the metallicity gradient evolution within disc galaxies is a consequence of a decrement of gas inflow rates from $z = 2$ to $z = 0$ and redistribution of gas within the galaxy disc. The observed metallicity gradients for disc galaxies within the SHiZELS survey do not support the trend predicted by the GIMIC simulation between $z = 0$ and $z = 2$. Nevertheless, we note that a much larger sample of disky galaxies at $z = 2$ are needed to further test this.

4 CONCLUSIONS

We present new AO-aided SINFONI IFU observations of spatially resolved Hα kinematics of 11 mass-selected ($M_{\star} = 10^{9.5\,-\,10.5}\,\mathrm{M}_{\odot}$) 'typical' star-forming galaxies from the wide-field narrow-band HiZELS survey in three redshift slices, $z = 0.8$, 1.47 and 2.23. All galaxies lie within <30 arcsec of bright ($R < 15.0$) stars enabling natural guide star AO-assisted observations. Modelling the Hα dynamics along the major kinematic axis of our galaxies, we derive a median dynamical-to-dispersion support of $V_{\mathrm{max}}\ \sin(i)/\sigma = 1.6 \pm 0.3$ (with a range of 1.1–3.8). We classify the galaxies using a kinemetry analysis (Shapiro et al. 2008) finding six disc-like galaxies and four mergers. One galaxy is unresolved. These new observations are combined with a previous similar study (nine galaxies taken from Swinbank et al. 2012a) to create a homogeneously selected sample of star-forming galaxies with dynamical characterization at $\sim$ kpc scales near the peak of the cosmic star formation rate density.

We find a tentative increase of the merger fraction as a function of redshift ($f_{\mathrm{merg}} \sim 0.0^{+0.4}$, $0.3^{+0.2}_{-0.2}$ and $0.6^{+0.2}_{-0.3}$ at $z = 0.8$, 1.47, 2.23, respectively). Nevertheless, our results are consistent with previous IFU surveys (Shapiro et al. 2008; Förster Schreiber et al. 2009), although we find higher merger fractions at a given sSFR in comparison to previous analyses by Stott et al. (2013a) who used a morphological classification from *HST* near-IR imaging.

We combine our observations with previous studies of intermediate and high-redshift galaxies (Swinbank et al. 2006; Cresci et al. 2009; Jones et al. 2010b; Gnerucci et al. 2011b; Miller et al. 2011, 2012; Swinbank et al. 2012a) to investigate the stellar mass TFR. We find that the scatter of this relation is affected by the galaxy pressure support (V/σ) – a result that is consistent with Tiley et al. (2016). On the other hand, we also investigate the $M_{\star}$–$S_{0.5}$ (Kassin et al. 2007) relation within the SHiZELS survey at $z = 0.8$–2.23. The kinematic measure $S_{0.5} = (0.5V^2 + \sigma^2)^{0.5}$ considers support by both rotational motions and dispersion arising from disordered motions (Weiner et al. 2006a). Our results are consistent (within 1σ) with the $M_{\star}$–$\mathrm{S}_{0.5}$ relationship found at $z \sim 0.2$, suggesting little or no evolution of this relation as function of redshift.

We measured the residuals from the 'FMR' (Stott et al. 2013b) at $z = 0.84$–1.47, finding that the scatter is consistent with measurements errors, suggesting no variation in the FMR up to $z = 2.23$.

We measure metallicity gradients ($\Delta\log_{10}(\mathrm{O/H})/\Delta R$) using the [N II]/H$\alpha$ ratio for 3, 7 and 2 galaxies at $z = 0.8$, 1.47 and 2.23 within the SHiZELS survey. These metallicity gradients range between -0.087 and 0.08 dex kpc^{-1}, with a median metallicity gradient of $\Delta\log_{10}(\mathrm{O/H})/\Delta R = -0.027 \pm 0.008$ dex kpc^{-1}. The evolution of metallicity gradients as a function of redshift in our modest sample at $z \leq 2$ does not exhibit any clear redshift trend such as the predicted by the GIMIC simulation for galaxy discs, where gas inflow rate decreases with decreasing redshift progressively. However, larger samples at $z = 2$ are needed to further test this.

We show that the metallicity gradient and global metallicity content are consistent with the anticorrelation suggested by Queyrel et al. (2012). This can be explained by the scenario in which infall of metal-poor gas from the IGM into the central part of the galaxy drives the positive gradients.

ACKNOWLEDGEMENTS

We thank to the anonymous referee for his/her careful read of the manuscript and helpful comments and suggestions. This work is based on observations collected at the European Organization for Astronomical Research in the Southern hemisphere under ESO programme ID 092.A-0090(A). This research was supported by CONICYT Chile (CONICYT-PCHA/Doctorado-Nacional/2014-21140483). AMS acknowledges an STFC Advanced fellowship, support from STFC (ST/L00075X/1) and the Leverhume foundation. IRS acknowledges support from STFC (ST/L00075X/1), the ERC Advanced Grant DUSTYGAL (321334) and a Royal Society/Wolfson Merit award. DS acknowledges financial support from the Netherlands Organization for Scientific research (NWO) through a Veni fellowship. PNB is grateful for support from STFC via grant ST/M001229/1.

REFERENCES

Alaghband-Zadeh S. et al., 2012, MNRAS, 424, 2232
Baldwin J., Phillips M., Terlevich R., 1981, PASP, 93, 5
Bellocchi E., Arribas S., Colina L., 2012, A&A, 542, 54
Bershady M. A., Verheijen M. A. W., Swaters R. A., Andersen D. R., Westfall K. B., Martinsson T., 2010, ApJ, 716, 198
Best P. et al., 2013, ASSP, 37, 235
Bluck A. F. L. et al., 2009, MNRAS, 394, 51
Bournaud F., Elmegreen B. G., 2009, ApJ, 694, L158
Bower R. G., Benson A. J., Malbon R., Helly J. C., Frenk C. S., Baugh C. M., Cole S., Lacey C. G., 2006, MNRAS, 370, 645
Bridge C. R. et al., 2007, ApJ, 659, 931
Bruzual G., 2007, in Vallenari A., Tantalo R., Portinari L., Moretti A. eds, ASP Conf. Ser. Vol. 374, From Stars to Galaxies: Building the Pieces to Build Up the Universe. Astron. Soc. Pac., San Francisco, p. 303
Bruzual G., Charlot S., 2003, MNRAS, 344, 1000
Calzetti D., Armus L., Bohlin R. C., 2000, ApJ, 533, 682
Chabrier G., 2003, PASP, 115, 763
Charbonneau P., 1995, ApJS, 101, 309
Cole S., Lacey C. G., Baugh C. M., Frenk C. S., 2000, MNRAS, 319, 168
Collins J. A., Rand R. J., 2001, ApJ, 551, 57
Conselice C. J., Bershady M. A., Dickinson M., Papovich C., 2003, AJ, 126, 1183
Conselice C. J., Rajgor S., Mywers R., 2008, MNRAS, 386, 909
Conselice C. J., Yang C., Bluck A. F. L., 2009, MNRAS, 394, 1956
Contini T. et al., 2012 A&A, 539, 91
Courteau S., 1997, AJ, 114, 2402
Crain R. A. et al., 2009, MNRAS, 399, 1773
Crain R. A. et al., 2015, MNRAS, 450, 1937
Cresci G. et al., 2009, ApJ, 697, 115
Davies R. et al., 2011, ApJ, 741, 69
Dekel A. et al., 2009a, Nature, 457, 451
Dekel A., Sari R., Ceverino D., 2009b, ApJ, 703, 785
Di Teodoro E. M., Fraternali F., Miller S. H., 2016, A&A, 594, A77
Dutton A. A. et al., 2011b, MNRAS 410, 1660
Edvardsson B., Andersen J., Gustafsson B., Lambert D. L., Nissen P. E., Tomkin J., 1993, A&A, 275, 101
Eisenhauer F. et al., 2003, in Iye M., Moorwood A. F. M., eds, Proc. SPIE Conf. Ser. Vol. 4841, Instrument Design and Performance for Optical/Infrared Ground-based Telescopes. SPIE, Bellingham, p. 1548
Elbaz D. et al., 2011, A&A, 533, A119
Elmegreen B. G., Elmegreen D. M., Fernandez M. X., Lemonias J. J., 2009, ApJ, 692, 12
Epinat B., Amram P., Balkowski C., Marcelin M., 2010, MNRAS, 401, 2113
Escala A., Larson R. B., 2008, ApJ, 685, 31
Fernández Lorenzo M. et al., 2009, A&A, 496, 389
Förster Schreiber N. M. et al., 2006, ApJ, 645, 1062
Förster Schreiber N. M. et al., 2009, ApJ, 706, 1364
Geach J. E., Smail I., Best P. N., Kurk J., Casali M., Ivison R. J., Coppin K., 2008, MNRAS, 388, 1473
Geach J. E., Smail I., Moran S. M., MacArthur L. A., Lagos C. d. P., Edge A. C., 2011, ApJ, 730, 19
Genzel R. et al., 2006, Nature, 442, 786
Genzel R. et al., 2010 MNRAS, 407, 2091
Genzel R. et al., 2011 ApJ, 733, 101
Gilbank D. G. et al., 2011, MNRAS, 414, 304
Glazebrook K., 2013, PASA, 30, 56
Gnerucci A. et al., 2011, A&A, 528, A88
Harrison C. M. et al., 2017, MNRAS, in press
Hung C. et al., 2015, ApJ, 803, 62
Ibar E. et al., 2013 MNRAS, 434, 3218
Jones T. A., Swinbank A. M., Ellis R. S., Richard J., Stark D. P., 2010b, MNRAS, 404, 1247
Karim A. et al., 2011, ApJ, 730, 61
Kassin S. A. et al., 2007, ApJ, 660, L35
Kennicutt R. C., Jr1998, ARA&A, 36, 189
Keres D., Katz N., Weinberg D. H., Davé R., 2005, MNRAS, 363, 2
Kewley L. J., Dopita M. A., Leitherer C., Davé R., Yuan T., Allen M., Groves B., Sutherland R., 2013, ApJ, 774, 100
Krajnović D., Cappellari M., de Zeeuw P. T., Copin Y., 2006, MNRAS, 366, 787
Kronberger T., Kapferer W., Schindler S., Ziegler B. L., 2007, A&A, 473, 761
Lacey C., Cole S., 1993, MNRAS, 262, 627
Lara-López M. A. et al., 2010, A&A, 521, L53
Lara-López M. A. et al., 2013, MNRAS, 434, 451
Larson K. L. et al., 2016, ApJ, 825, 128
Law D. R., Steidel C. C., Erb D. K., Larkin J. E., Pettini M., Shapley A. E., Wright S. A., 2009, ApJ, 697, 2057
Lin L. et al., 2008, ApJ, 681, 232
Lotz J. M., Primack J., Madau P., 2004, AJ, 128, 163
Lotz J. M. et al., 2008, ApJ, 672, 177
Madau P., Ferguson H. C., Dickinson M. E., Giavalisco M., Steidel C. C., Fruchter A., 1996, MNRAS, 283, 1388
McCarthy I. G., Font A. S., Crain R. A., Deason A. J., Schaye J., Theuns T., 2012, MNRAS, 420, 2245
Mannucci F., Cresci G., Maiolino R., Marconi A., Gnerucci A., 2010, MNRAS, 408, 2115
Miller S. H., Bundy K., Sullivan M., Ellis R. S., Treu T., 2011, ApJ, 741, 115
Miller S. H., Ellis R. S., Sullivan M., Bundy K., Newman A. B., Treu T., 2012, ApJ, 753, 7
Mo H. J., Mao S., White S. D. M., 1998, MNRAS, 295, 319
Noeske K. G. et al., 2007, ApJ, 660, L43
Osterbrock D. E., 1989, Astrophysics of Gaseous Nebulae and Active Galactic Nuclei. University Science Books, Mill Valley, CA
Pannella M. et al., 2009, ApJ, 698, L116
Pettini M., Pagel B. E. J., 2004, MNRAS, 348, L59
Pizagno J. et al., 2005, ApJ, 633, 844
Queyrel J. et al., 2012, A&A, 539, A93
Rodighiero G. et al., 2011, ApJ, 739, L40
Shapiro K. L. et al., 2008, ApJ, 682, 231
Sobral D. et al., 2009, MNRAS, 398, 75
Sobral D., Best P. N., Geach J. E., Smail I., Cirasuolo M., Garn T., Dalton G. B., Kurk J., 2010, MNRAS, 404, 1551
Sobral D., Best P. N., Smail I., Geach J. E., Cirasuolo M., Garn T., Dalton G. B., 2011, MNRAS, 411, 675
Sobral D., Best P. N., Matsuda Y., Smail I., Geach J. E., Cirasuolo M., 2012, MNRAS 420, 1926
Sobral D. et al., 2013b, ApJ, 779, 139
Sobral D. et al., 2013c, MNRAS, 428, 1128
Sobral D., Best P. N., Smail I., Mobasher B., Stott J., Nisbet D., 2014, MNRAS, 437, 3516
Sobral D. et al., 2015, MNRAS, 451, 2303
Sobral D., Kohn S. A., Best P. N., Smail I., Harrison C. M., Stott J., Calhau J., Matthee J., 2016, MNRAS, 457, 1739

Springel V. et al., 2005, Natur, 435, 629
Stott J. et al., 2013a, MNRAS, 436, 1130
Stott J., Sobral D., Smail I., Bower R., Best P. N., Geach J. E., 2013b, MNRAS, 430, 1158
Stott J. et al., 2014, MNRAS, 443, 2695
Stott J. P. et al., 2016, MNRAS, 457, 1888
Swinbank A. M., Bower R. G., Smith G. P., Smail I., Kneib J.-P., Ellis R. S., Stark D. P., Bunker A. J., 2006, MNRAS, 368, 1631
Swinbank A. M., Sobral D., Smail I., Geach J. E., Best P. N., McCarthy I. G., Crain R. A., Theuns T., 2012a, MNRAS, 426, 935
Swinbank A. M., Smail I., Sobral D., Theuns T., Best P. N., Geach J. E., 2012b, ApJ, 760, 130
Swinbank A. M. et al., 2015, ApJ, 806, 17
Thompson A. P. et al., 2017, ApJ, in press
Tiley A. L. et al., 2016, MNRAS, 460, 103
Tissera P. B., Pedrosa S. E., Sillero E., Vilchez J. M., 2016, MNRAS, 456, 2982
Tully R. B., Fisher J. R., 1977, A&A, 54, 661
van Starkenburg L., van der Werf P. P., Franx M., Labbé I., Rudnick G., Wuyts S., 2008, A&A, 488, 99
Vergani D. et al., 2012, A&A 546, 118
Weiner B. J. et al., 2006a, ApJ, 653, 1027
Wisnioski E. et al., 2011, MNRAS, 417, 2601

APPENDIX A: SERENDIPITOUS DETECTION

Within the SA22-26 data cube we found an unexpected emission line at $\lambda \sim 1.203$ μm. This emission line does not coincide with any expected emission line emitted from the SA22-26 source as it corresponds to $\lambda_{\rm rest} \sim 0.663$ μm in this galaxy's rest frame. This unexpected emission line overlaps spatially with part of the Hα emission from SA22-26 source (Fig. A1-*top*). Furthermore, the kinematical behaviour of this emission line region shows a PA (Fig. A1-*bottom*) that differs from the PA derived for the SA22-26 source (Fig. 3). This suggest that this serendipitous emission does not come from SA22-26. We did not find any other emission lines associated with this galaxy which could be used for determining the redshift of this possible new source. We call this source as SA22-26B. If we assume that this emission line is also a redshifted Hα emission line, then SA22-26B is offset redwards by $\sim$5500 km s^{-1} (in the line-of-sight direction, $z \sim 0.833$) from the SA22-26 source. The modest redshift difference if the emission line is Hα would be consistent with no lensing. We note that the emission from SA22-26 shows no sign of extinction by SA22-26B supporting the fact that this galaxy is background.

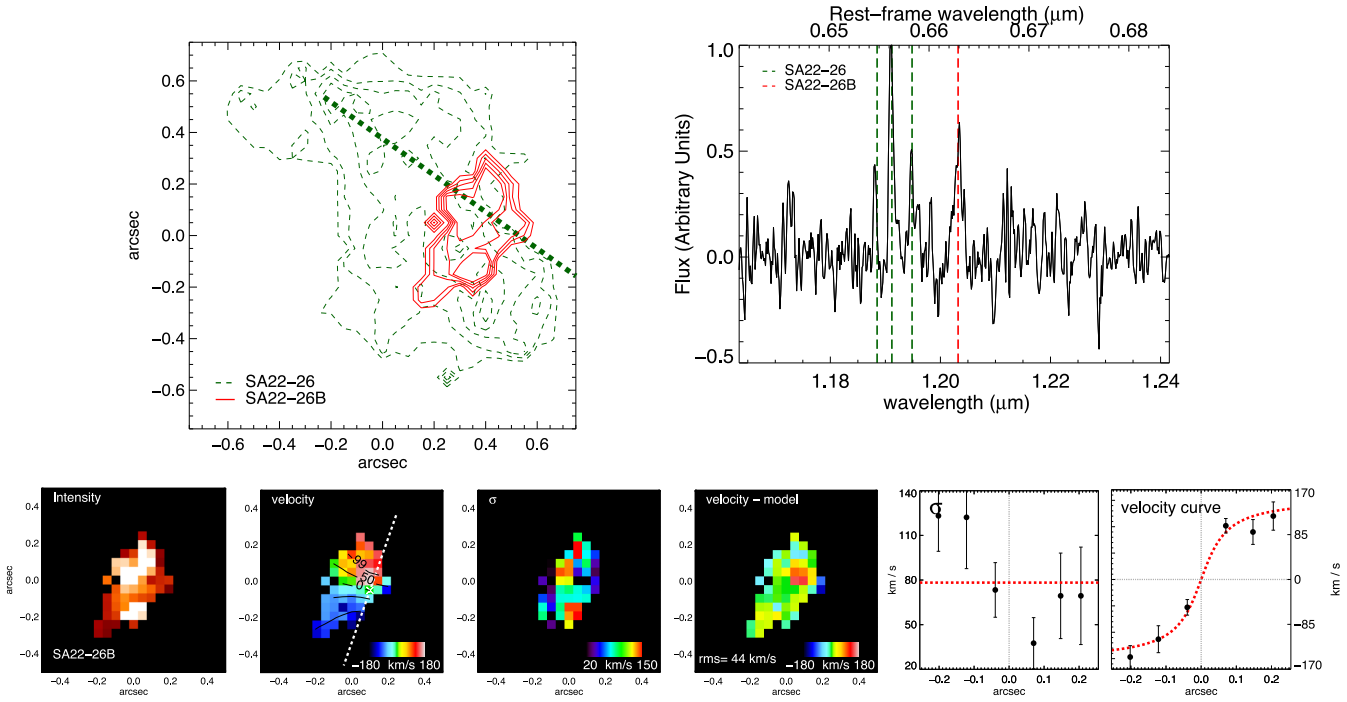

Figure A1. *Top left*: Intensity contours of our serendipitous detection (red) and SA22-26 (green-dashed) sources within the SINFONI data cube. The dashed line shows the PA derived for SA22-26 source. There is a clear spatially overlap between both emissions. *Top right*: Spatially integrated one-dimensional spectra of SA22-26B. The emission is integrated within the red contour showed in top-left figure. The red-dashed line shows the emission line detected at $\lambda \sim 1.203$ μm. The green-dashed lines show the Hα, [N II]$\lambda\lambda$6583, 6548 emission lines for the SA22-26 source extracted from the same area. *Bottom*: Intensity, velocity, line-of-sight velocity dispersion (σ), residual field, one-dimensional velocity dispersion profile and one-dimensional velocity profile (as in Fig. 3) for our serendipitous detection. The spatial scale is showed in arcseconds due to the uncertain redshift determination.

This paper has been typeset from a TEX/LATEX file prepared by the author.